

# UC Berkeley

## UC Berkeley Previously Published Works

### Title

EQSIM—A multidisciplinary framework for fault-to-structure earthquake simulations on exascale computers, part II: Regional simulations of building response

### Permalink

<https://escholarship.org/uc/item/4605k75t>

### Journal

Earthquake Spectra, 37(2)

### ISSN

8755-2930

### Authors

McCallen, David  
Petrone, Floriana  
Miah, Mamun  
et al.

### Publication Date

2021-05-01

### DOI

10.1177/8755293020970980

Peer reviewed

# EQSIM—A multidisciplinary framework for fault-to-structure earthquake simulations on exascale computers, part II: Regional simulations of building response

Earthquake Spectra

1–26

© The Author(s) 2020

Article reuse guidelines:

[sagepub.com/journals-permissions](https://sagepub.com/journals-permissions)

DOI: 10.1177/8755293020970980

[journals.sagepub.com/home/eqs](https://journals.sagepub.com/home/eqs)

David McCallen, M.EERI<sup>1,2</sup>, Floriana Petrone, M.EERI<sup>1,2</sup>, Mamun Miah<sup>2</sup>, Arben Pitarka<sup>3</sup> , Arthur Rodgers<sup>3</sup>, and Norman Abrahamson<sup>4</sup>

## Abstract

The existing observational database of the regional-scale distribution of strong ground motions and measured building response for major earthquakes continues to be quite sparse. As a result, details of the regional variability and spatial distribution of ground motions, and the corresponding distribution of risk to buildings and other infrastructure, are not comprehensively understood. Utilizing high-performance computing platforms, emerging high-resolution, physics-based ground motion simulations can now resolve frequencies of engineering interest and provide detailed synthetic ground motions at high spatial density. This provides an opportunity for new insight into the distribution of infrastructure seismic demands and risk. In the work presented herein, the EQSIM fault-to-structure computational framework described in a companion paper, McCallen et al., is employed to investigate the regional-scale response of buildings to large earthquakes. A representative  $M = 7.0$  strike-slip event is used to explore the distribution and amplitude of building demand, and comparisons are made between building response computed with fault-to-structure simulations and building response computed with existing measured near-fault earthquake records. New information on the distribution and variability of building response from high-performance parallel simulations is described and analyzed, and favorable

<sup>1</sup>University of Nevada, Reno, Reno, NV, USA

<sup>2</sup>Lawrence Berkeley National Laboratory, Berkeley, CA, USA

<sup>3</sup>Lawrence Livermore National Laboratory, Livermore, CA, USA

<sup>4</sup>University of California, Berkeley, Berkeley CA, USA

## Corresponding author:

David McCallen, University of Nevada, Reno, 1664 North Virginia Street, Reno, NV 89557, USA.

Email: [dmccallen@unr.edu](mailto:dmccallen@unr.edu)

first comparisons between building response predicted with both fault-to-structure simulations and real ground motions records are presented.

### **Keywords**

High-performance computing, exascale computers, fault-to-building simulations, regional building response, building demand variability

Date received: 6 May 2020; accepted: 28 September 2020

## **Introduction**

Earthquake processes, starting with fault rupture, continuing through seismic wave propagation to the site of interest, and finally the interaction between complex incident waves and soil–structure systems, result in significant spatial variation in ground motion and infrastructure response. Much work remains to be done to develop a full understanding and reduce uncertainties in the prediction of such regional distributions of infrastructure risk. Observational data are, and will continue to be, very limited because there is often no historical ground motion data from large earthquakes for regions of interest, for example, the last major earthquake on the Hayward fault in Northern California occurred in 1868, well before the first seismic stations were installed. Even where earthquakes have been observed, the seismic instrumentation used to measure the ground motion and structural response is sparse, further emphasizing the challenges associated with drawing conclusions from limited empirical data. This situation is particularly acute in the near-fault region where observational data are even more limited.

With the rapid developments in high-performance computational capabilities, and the increasing understanding of the physics underlying earthquake phenomenon, the ability to simulate these complex processes continues to advance. With the advent of petaflop and pending exaflop computers, Alexander et al. (2020), high-frequency ground motion simulations can, for the first time, be performed to resolve frequencies of relevance to engineered systems. High-performance simulations can provide spatially dense information on ground motions and infrastructure response at regional scale, yielding information for new insights into the response of engineering structures, and new data for risk-informed, performance-based earthquake engineering. In addition, the ability to simulate realistic three-dimensional ground motion waveforms and appropriately couple geophysics and engineering simulation models can provide new information on the interplay between infrastructure systems and complex, three-dimensional incident wavefields.

Previous examples of the extension of regional ground motion simulations to include the analysis of infrastructure systems have been performed by Taborda and Bielak (2011), Isbiloglu et al. (2015), Bijelic et al. (2019), Zhang et al. (2019), and Sahin et al. (2016). This article describes recent applications of the EQSIM fault-to-structure computational framework for regional-scale earthquake hazard and risk assessments and evaluations of the characteristics of the resulting synthetic ground motions and structural response.

## **Regional simulations for a representative strike-slip fault**

When developing the first computational models of complex systems and processes, it is essential to both qualitatively and quantitatively evaluate model predictions to assess the realism and build confidence in numerical results. To allow investigation of the distribution

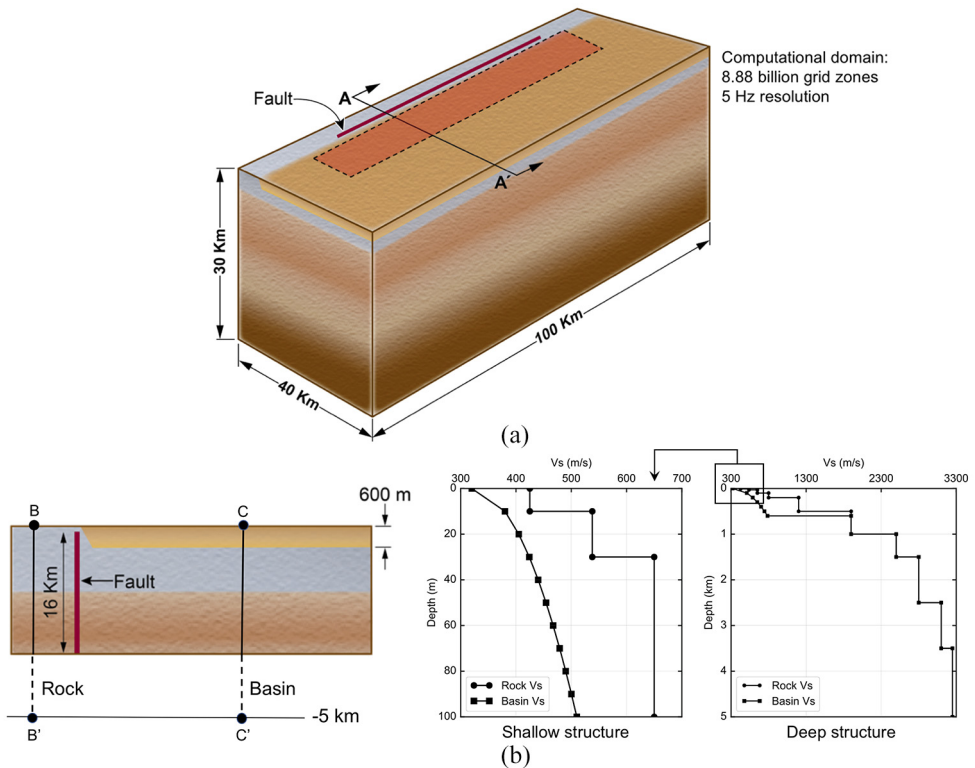


**Figure 1.** A representative regional-scale model of a rock-basin domain: (a) extent of the regional model and location of a strike-slip fault adjacent to the basin; (b) geologic velocity structure with depth for rock and basin sites.

of synthetic ground motions and infrastructure response with the EQSIM framework, a regional model of a representative strike-slip fault located adjacent to a sedimentary basin was investigated as shown in Figure 1. This generic model was deliberately created to allow exploration of building response with a relatively simple model, including a fully characterized geologic structure, executable with reasonable run times to allow exploration of the parametric space. Such a model provides insight into how fault-rupture influences the spatial variability of building response in the near field of a large earthquake where the details of the rupture, and the corresponding radiation pattern, can result in large variability of seismic demand on identical buildings located at different sites in the near-field. For the purpose of this study, near-fault ground motions and structural response were evaluated in detail for the sedimentary basin side of the fault for a rectangular region encompassing all sites within 10 km of the fault (the orange rectangle in Figure 1a).

A three-dimensional computational earth model was constructed for the regional domain representing the shallow sedimentary basin with a maximum depth of 600 m. As shown in Figure 1, the shear wave velocity in the basin gradually increases with depth from 320 m/s at the free surface to 800 m/s at the base. The seismic velocity model is automatically mapped into a computational grid by internal subroutines utilized by the SW4 program, Nilsson et al. (2007), Sjogreen and Petersson (2012), and Petersson and Sjogreen (2012), as described in a companion paper, McCallen et al. (in press). The earth model

**Table 1.** Computational metrics of one regional-scale fault-rupture ground motion simulation on the Cori computer

<i>M</i> = 7 fault-rupture simulation with the EQSIM SW4 model	
Ground motion frequency resolution	5 Hz
Number of grid points	$8.88 \times 10^9$
Number of CORI compute nodes utilized/CPU (64 CPUs per node)	2048 compute nodes/131,072 CPUs
Duration of earthquake motions/time step/no. of steps	90 s/0.002257/39,876
Wall clock time for one <i>M</i> = 7 event simulation	5 h 23 min

included 8.88 billion grid points to resolve ground motion frequencies up to 5 Hz, and the Cartesian grid employed mesh refinement with depth to maintain numerical accuracy for 5 Hz simulations with grid spacings of 8, 16, and 32 m in the depth ranges 0–600 m, 600–1200 m, and below 1200 m, respectively. For each earthquake rupture scenario, 90 s of simulated earthquake motion was computed in an approximately 5 h run time on Cori, a 30 Petaflop supercomputer at the National Energy Research Scientific Computing Center at Lawrence Berkeley National Laboratory (<https://www.nersc.gov/systems/cori/>) as summarized in Table 1. The ability to compute a full regional earthquake scenario in approximately 5 h allows the exploration of the problem parameter space on reasonable time scales.

As described in a companion paper, the physics-based method of Graves and Pitarka (2016) (GP, hereafter), including recent improvements for hybrid representation of spatial slip by Pitarka et al. (2020a), was used to generate kinematic models of rupture scenarios for a M7 strike-slip earthquake on a fault that ruptures to the surface. The fault length is 62.5 km, and the fault depth is 16 km. Rupture parameters were estimated using empirical relations between the seismic moment and fault area for strike-slip earthquakes proposed by Leonard (2010). In the GP model, the rupture characteristics, including spatial and temporal variations of slip, slip rate, and rupture speed, are constrained from dynamic rupture modeling and validated against recorded near-fault ground motions and ground motion prediction equations (Dreger et al., 2015; Pitarka et al., 2020a; Pitarka et al., 2020b).

The three rupture scenarios developed for the simulations have the same slip distribution but different rupture initiation. Figure 2 illustrates the first kinematic rupture scenario in which the rupture initiates near the left end of the fault. This figure displays the slip distribution, rise time, and rupture times resulting from the rupture kinematics. The average slip is 122 cm and the maximum slip is 488 cm. Note the spatial correlation between the slip and rise time, as well as the strong dependency of rise time with depth. These two important rupture characteristics impact the frequency content of the near-fault ground motion: the impulsive characteristics of ground velocity and permanent displacement along the fault. In the second rupture scenario, the rupture initiates in the center, and in the third scenario, the rupture initiates near the right end of the fault. The selection of rupture initiation points for each scenario was made in order to produce strong near-fault-rupture directivity effects for predominantly unilateral ruptures (first and third scenarios) and weaker directivity effect for a bilateral rupture (second scenario).

As a basis for comparison between the recorded and simulated ground motions, measured near-fault records were obtained from the database of pulse-like, near-fault motion records developed by Baker et al. (2011; <https://peer.berkeley.edu/research/transportation->

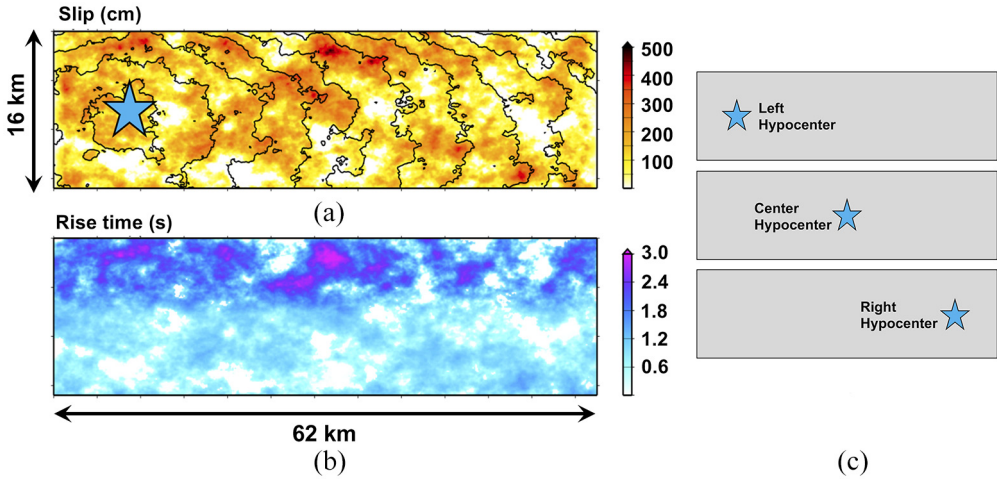


**Figure 2.** Fault-rupture model for a M7 strike-slip earthquake: (a) Slip distribution across the fault plane with the location of the hypocenter; (b) rise time distribution across the fault plane; (c) hypocenter locations for all rupture scenarios considered.

systems/ground-motion-studies-transportation-systems) and summarized in Table 2. For each site, the ground motions have been rotated into the fault-normal and fault-parallel components. As the database of near-fault records from any one earthquake is very limited in terms of the number of ground motion recordings, the ground motions from these multiple events were combined into a single data set. The average earthquake magnitudes and site conditions of the simulated and real records are quite similar, with an  $M = 7$  for the simulations versus an average magnitude of  $M = 7.1$  for real records and an average site  $V_{s30}$  of 382 m/s for the simulation model sites versus a median  $V_{s30}$  of 366 m/s for the actual earthquake record sites.

For the left most hypocenter, time snapshots of the waves propagating from the earthquake rupture front, with color coding according to ground velocity amplitude, are shown in Figure 3. From these plots and animations of the wave propagation as the waves traverse from the hypocenter toward the right end of the fault, a significant forward directivity effect is evident. Selected simulated ground motion waveforms for this rupture scenario are shown in Figures 4 and 5. Figure 4 shows the ground motion waveforms for three selected sites (A, B, and C) each at a distance of 1 km from the fault rupture, and Figure 5 shows the reduction in ground motions as distance increases from the fault (sites B, C, and D). The synthetic ground motion waveforms illustrate both representative fault-parallel fling step (Point B fault-parallel motion) and a fault-normal forward directivity pulse (Point B fault-normal motion) as shown in Figure 4, and they qualitatively agree with expected near-fault waveforms (Gazetas et al., 2009). In addition, the simulated ground motion records are fully broad band from 0 to 5 Hz, so unlike band limited measured ground motion records the ground displacements associated with the permanent fault displacement are fully represented in the simulations.

For the 2490 synthetic ground motion records (830 sites within 10 km of the fault  $\times$  3 rupture scenarios) and the 38 real records for sites within 10 km of the fault, pseudo-acceleration and pseudo-velocity response spectra were computed and are compared in

**Table 2.** Database of pulse-like, near-fault measured records for sites within 10 km of a major fault rupture, from (Baker et al., 2011)

Earthquake	<i>M</i>	Year	Station	Rupture distance (km)	<i>V</i> <sub>s30</sub> (m/s)
Morgan Hill	6.19	1984	Coyote Lake Dam	0.53	597.1
Imperial Valley-06	6.53	1979	EC Meloland Overpass FF	0.07	186.2
			EC County Center FF	7.31	192.1
			El Centro Differential Array	5.09	202.3
			El Centro Array 6	1.35	203.2
			El Centro Array 5	3.95	205.6
			El Centro Array 8	3.86	206.1
			El Centro Array 4	7.05	208.9
			El Centro Array 7	0.56	210.5
Northridge-01	6.69	1994	Sylmar—Converter Sta	5.35	251.2
			Newhall—Fire Sta	5.92	269.1
			Rinaldi Receiving Sta	6.50	282.3
			Newhall—W Pico Canyon Rd.	5.48	285.9
			Sylmar—Converter Sta East	5.19	370.5
			Jensen Filter Plant	5.43	373.1
			Sylmar—Olive View Med FF	5.30	440.5
			Jensen Filter Plant Generator	5.43	525.8
Kobe, Japan	6.90	1995	KJMA	0.96	312.0
			Takarazuka	0.27	312.0
Loma Prieta	6.93	1989	LGPC	3.88	477.7
			Gilroy—Gavilan Coll.	9.96	729.7
Landers	7.28	1992	Lucerne	2.19	684.9
Chi-Chi, Taiwan	7.62	1999	CHY101	9.96	258.9
			WGK	9.96	258.9
			TCU101	2.13	272.6
			TCU053	5.97	454.6
			TCU054	5.30	460.7
			TCU082	5.18	472.8
			TCU087	7.00	473.9
			TCU122	9.35	475.5
			TCU049	3.78	487.3
			TCU068	0.32	487.3
			TCU103	6.10	494.1
			CHY028	3.14	542.6
			TCU075	0.91	573.0
			TCU052	0.66	579.1
			TCU076	2.76	615.0
			TCU102	1.51	714.3

Figure 6. Both the scatter distribution of the spectra from the synthetic and real records and the median spectra— $\exp(\mu_{lnSa})$  and  $\exp(\mu_{lnSv})$ —obtained from the synthetic and real records demonstrate reasonable agreement in terms of shape, amplitude, and frequency content.

For this particular fault-rupture model and related rupture scenarios, there is a tendency for the median synthetic spectra to be slightly higher than the median real record spectra in the high-frequency region and slightly lower in the low-frequency region. It is also noted that the Chi-Chi earthquake provides the largest number of stations in the real record database (16 of the 38 records), and Chi-Chi was noteworthy due to the fact that accelerations were generally lower than observed at short distances for other large magnitude events (Sommerville, 2003; Somerville and Pitarka, 2006). With the heavy

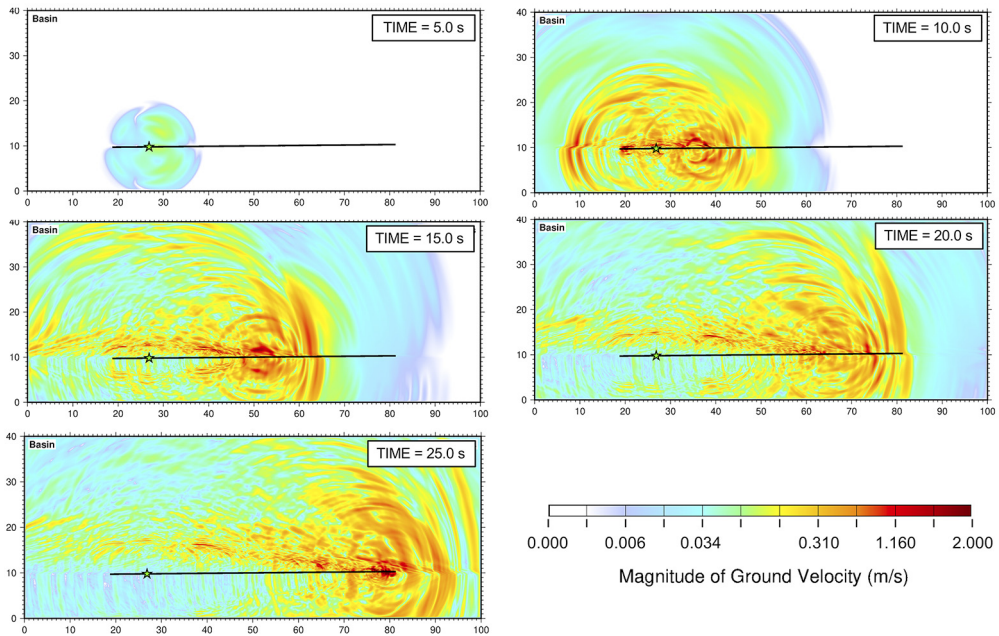


**Figure 3.** Waves propagating from the rupturing fault (left hypocenter) with a forward directivity effect to the right.

weighting of the database toward the Chi-Chi event, there is a tendency to push the short period median spectral values of the real records downward. An evaluation of the realism of this set of synthetic ground motions for applications in engineering domains is presented in Petrone et al. (2020)

### Building response characteristics and intra-event variability

To evaluate the amplitude and distribution of building response to ground motions, contemporary steel moment frame buildings of various heights were considered (Astaneh-Asl, 2018) and detailed nonlinear building models were created for each of the planar buildings as described in McCallen et al. (in press) and Wu et al. (2019). The NEVADA implicit, finite deformation, nonlinear finite element program, which contains a fiber beam model with a co-rotational coordinate system, was employed to model building nonlinear response (McCallen and Larsen, 2003; Petrone et al., 2016). The natural frequencies of the representative steel frame buildings are summarized in Table 3 with the fundamental mode periods spanning a significant range from 0.606 to 3.76 s.

The database of surface ground motions at 1 km spacing throughout the entire regional domain includes  $99 \times 39 = 3861$  stations for a total of  $3861 \times 3 = 11,583$  seismograms for all three scenarios. Each of the four representative buildings was analyzed for the synthetic ground motions at each station on the surface for both fault-normal and fault-parallel components of ground motion resulting in  $11,583 \times 2 \times 4 = 92,664$  nonlinear building time history analyses. The compute time for the nonlinear analyses for one particular building was small compared to the ground motion simulation with in the order of 1/10th the computer node-hour requirements of the ground motion simulation.



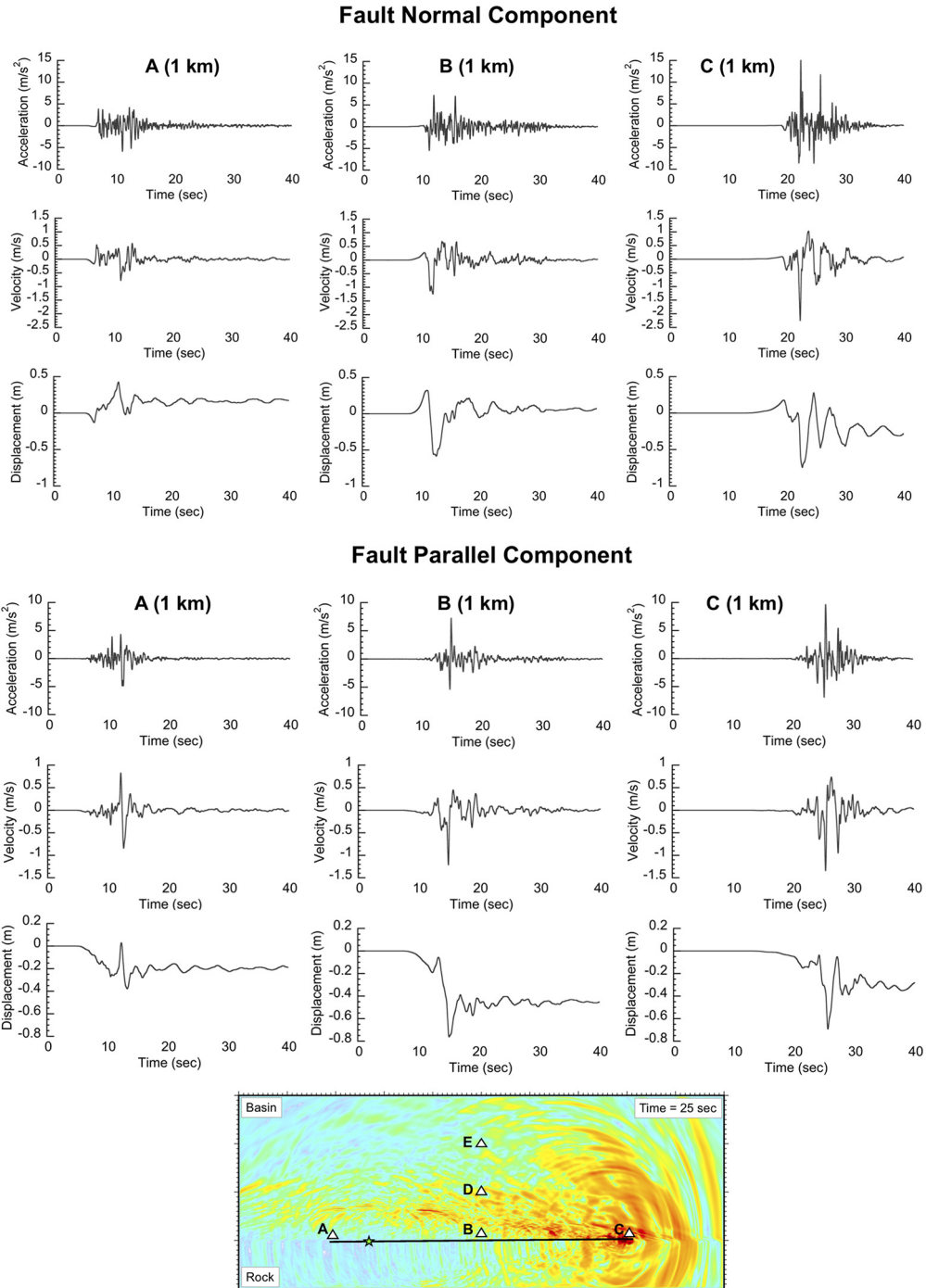


**Figure 4.** Computed fault-normal and fault-parallel ground motions for sites 1 km off the fault (to 5 Hz resolution): stations ABC.

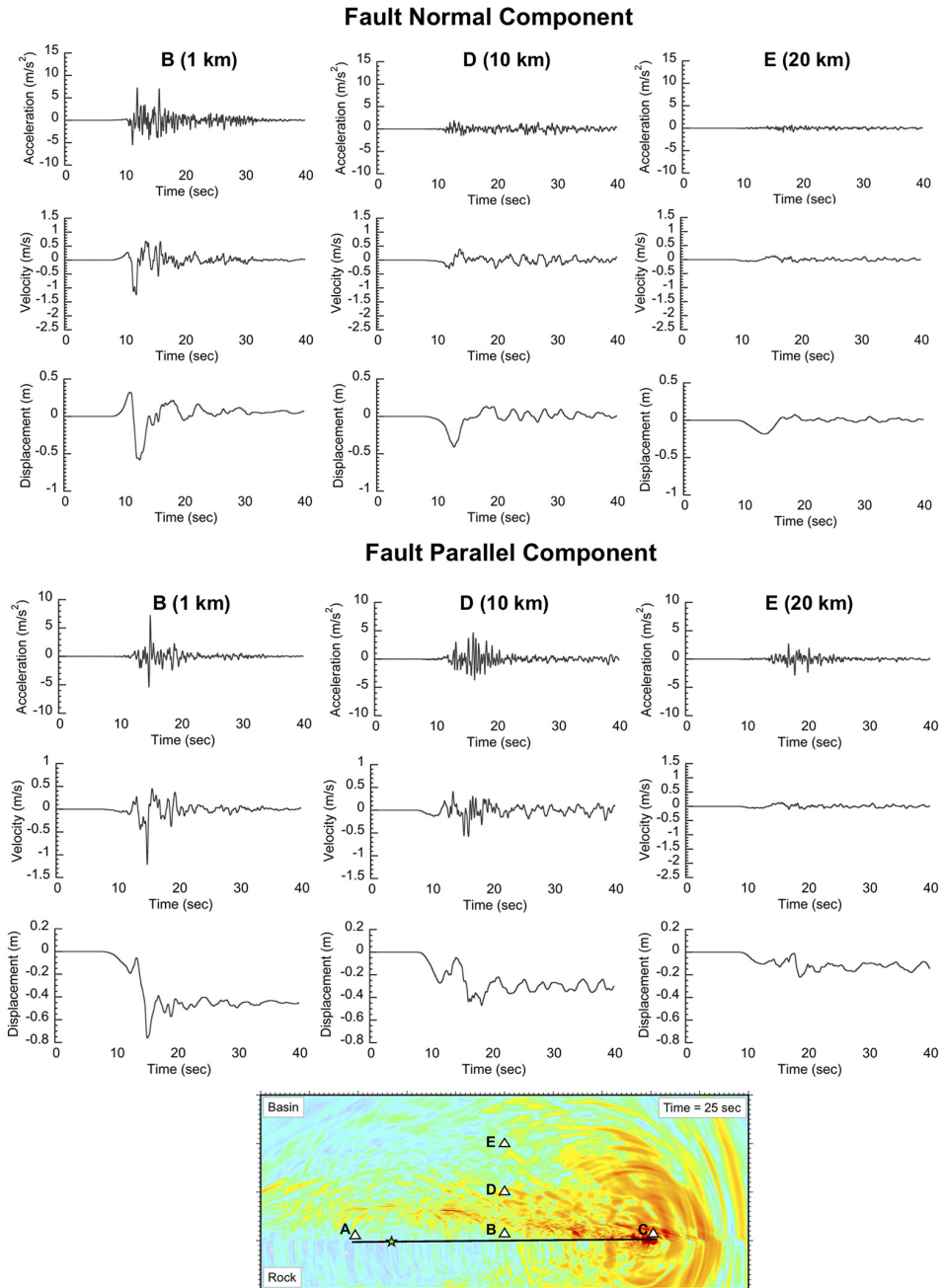


**Figure 5.** Amplitude reduction of computed ground motions with distance from the fault (to 5 Hz resolution): stations BDE.

To provide a quantitative measure of building demand for each building simulation at each site, the peak interstory drift (PID) ratio occurring at any story in the building was determined for each simulated time history. To characterize the earthquake demand on each building at each site, the PID ratio-based limit states for steel moment frame

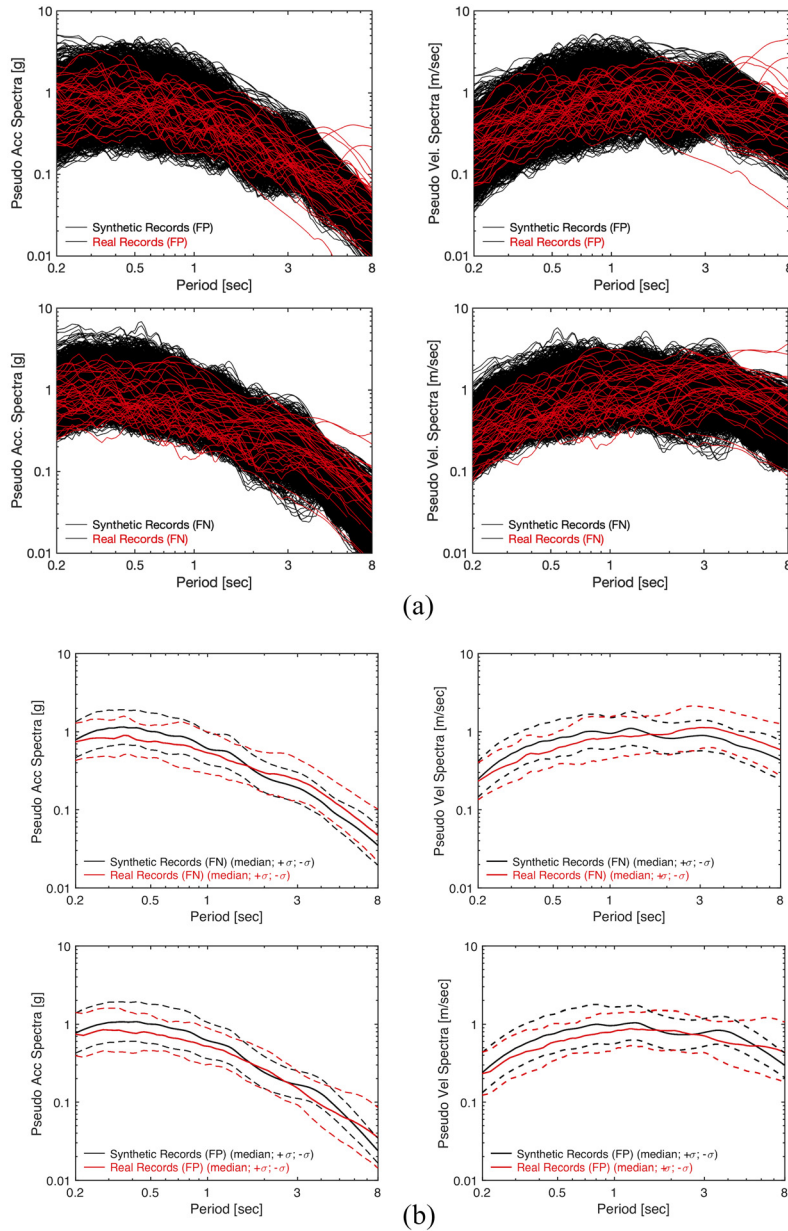


**Figure 6.** Response spectra comparison for synthetic (2490) and real (38) ground motions for each component: (a) Spectral scatter of all synthetic and real records for fault-normal and fault-parallel components; (b) median spectra for fault-normal and fault-parallel components.

buildings from the American Society of Civil Engineers Standard 43-05, ASCE/SEI 43-05 (ASCE, 2005), are used. The limit states for this standard, broadly used for a breadth of U.S. Department of Energy structures and facilities, are summarized in Table 4.

To express the regional distribution of building response throughout the domain of the computational model, the PID from the rupture-to-building simulations at each surface

**Table 3.** Natural modes of four representative steel moment frame buildings

Building	Mode 1	Mode 2	Mode 3
	Period Frequency	Period Frequency	Period Frequency
Three story	0.606 s	0.191 s	0.097 s
	1.65 Hz	5.24 Hz	10.34 Hz
Nine story	2.13 s	0.734 s	0.410 s
	0.469 Hz	1.36 Hz	2.44 Hz
Twenty story	2.68 s	0.915 s	0.521 s
	0.373 Hz	1.09 Hz	1.918 Hz
Forty story	3.76 s	1.37 s	0.815 s
	0.266 Hz	0.732 Hz	1.23 Hz

**Table 4.** Upper bounds on drift defined limit states for moment frame buildings (ASCE 43-05)

Structural system	Limit State A <i>Large permanent distortion</i>	Limit State B <i>Moderate permanent distortion</i>	Limit State C <i>Limited permanent distortion</i>	Limit State D <i>Essentially elastic behavior</i>
Steel frame	3.5%	2.5%	1.0%	0.5%
Concrete frame	2.5%	1.5%	1.0%	0.5%

site was established and classified according to the corresponding ASCE 43-05 limit states. The 1 km pixel associated with each building site was color coded according to the limit state associated with the PID obtained from the nonlinear building simulation at the site (Figure 7a). Subsequently, continuous smooth contours of the various limit states were developed as shown in Figure 7b.

The building response data are summarized in Figures 8–11. Each figure shows the following:

- The building PID ratio limit state contours for the left hypocenter rupture scenario (see Figure 2) for the entire computational domain.
- The PID ratio vs Sa(T1) scatter plot combining data from all three hypocenter rupture scenarios for the stations located within 10 km of the fault rupture (region delimited by the dotted black line) and real records.
- The PID ratio histogram fit with lognormal distributions for simulated records from all three hypocenter rupture scenarios for the stations located within 10 km of the fault rupture (region delimited by the dotted black line) and for real records, with corresponding statistics (median and standard deviation, the latter in natural log units).

For each building, the top panel of each figure shows the fault-normal (FN) component and the bottom panel shows the fault-parallel (FP) component.

The limit state contour plots illustrate a complex regional distribution of drift, with buildings equidistant from the fault rupture exhibiting PID ratios ranging from LS-C to LS-A (ASCE 43-05). Inspection of the PID vs Sa(T1) scatter plots provides a clear visual representation of how the response from synthetic and real records correlate in terms of

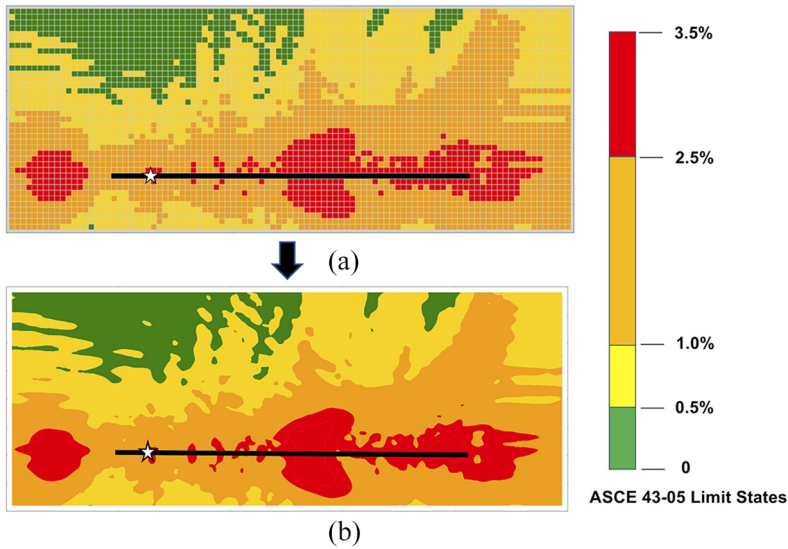


**Figure 7.** Discrete site building drifts for a nine-story building by ASCE 43-05: (a) Limit states for each grid pixel; (b) discrete limit states translated into continuous limit state drift contours.

amplitude of PID ratio and the scatter of PID resulting from the contribution of higher modes and nonlinearities in the structural response. Finally, the analysis of how the populations of building response are statistically distributed shows to what extent the demand imposed on the structures by the synthetic records and the real records is in reasonable agreement not only in terms of median value of the PID ratio— $\exp(\mu_{\ln PID})$ , but also in terms of standard deviation— $\sigma_{\ln PID}$ , which provides an objective indicator of the variability of the PID ratio in the considered near-fault domain (region delimited by the dotted black line). The comparison of distribution of PID for the real records and the simulations is not a quantitative validation of the simulations because the real records are for different crustal structures than used in the simulations and they are from a range of earthquake magnitudes and mechanisms. The comparison is used to show that the results of the simulations are reasonable in terms of the median and variability of the PID.

In all cases, the median and standard deviation of PID ratio from synthetic ground motions are reasonably consistent with those from the real near-fault ground motion records. The differences range between  $-0.18$  and  $+0.08$  natural log units in the standard deviation, as shown in Table 5. Negative differences in the standard deviation are indicative of an underestimate of the variability of the PID ratio from the simulations compared to the real records, whereas positive values are indicative of an overestimation of the variability.

For the left hypocenter rupture scenario and all four buildings, the maximum PID due to FN motion is achieved near the right end of the fault at the station closest to the fault (1 km), as shown in Figures 8a through 11a. This results from the strong fault-normal directivity pulse created by the left side hypocenter as the fault rupture propagates toward the right end of the fault (Figure 3). For all four buildings, this  $M = 7.0$  earthquake results in localized hot-spots where the building PID extends into the LS-A, the drift region associated with large permanent deformation of the ASCE 43-05 limit state criteria.

**Table 5.** Differences in building median and standard deviation of PID for synthetic and real ground motions

Building	Fault-normal component		Fault-parallel component	
	$(PID_{syn}-PID_{real})/PID_{syn}$ % diff	$(\sigma_{syn}-\sigma_{real})$ (natural log units)	$(PID_{syn}-PID_{real})/PID_{syn}$ % diff	$(\sigma_{syn}-\sigma_{real})$ (natural log units)
Three story	+ 17%	-0.05	+ 18%	0.06
Nine story	-5%	-0.18	+ 1%	0.04
Twenty story	-13%	-0.16	+ 9%	0.08
Forty story	-8%	-0.07	+ 19%	0.01

For the nonlinear building models, the time evolution of the story drift at the location of maximum PID within the 10 km zone of the fault are shown in Figures 12 and 13. The models exhibit significant inelastic behavior for these sites, which correlates with the ASCE limit state description. In general, for these contemporary structures, the taller buildings tend to exhibit more localized inelastic zones, often with peak drift higher in the building, while the shorter buildings exhibit more broadly distributed inelastic demand. Animation of the tall building response illustrates what are essentially higher mode contributions that result in large drifts in the top third of the building when the near-fault ground motion pulse arrives at the building site, similar to the type of near-fault response described by Alavi and Krawinkler (2004).

To further illustrate the variability of response of the building systems, the range and distribution of building drift for equidistant lines parallel to the fault and located at 1, 5, 10, 15, 20, 25 and 29 km from the fault are shown in Figures 14 and 15 for the three-story and forty-story buildings, respectively. Each figure shows the PID ratio histogram generated over a population of  $63 \times 3 = 189$  values (along each line parallel to the fault) and the fit with lognormal distributions with the corresponding statistics,  $\exp(\mu_{\ln PID})$  and  $\sigma_{\ln PID}$ , for FP and FN components. Table 6 summarizes the results from all buildings and for both components and shows the ratio of the median PID at 1 km off the fault to the median PID at 29 km off the fault along with the corresponding variation in the standard deviation.

The PID values from the plots and from Table 6 show that when moving from sites located at 29 km off the fault rupture to sites located at 1 km off the fault rupture, the median PID varies by a factor as high as 9.35 for the three-story building in the FN component, confirming the higher demand posed to near-fault structures. The small variation in the standard deviation, with a maximum value of 0.13 observed in the nine-story building for the FP component, demonstrates that the variability of PID for sites equidistant from the fault rupture characterizes almost equally all station lines located up to 29 km off the fault rupture. However, for stations located at 29 km off the fault rupture, the PID ratios vary within the LS-D, whereas for stations located at 1 km off the fault rupture the PID ratios extend up to LS-A, which overall has significant implications for understanding the range and variability of damage to a specific building for a major earthquake. As these results are the first in-depth evaluation with the EQSIM framework progressing all the way from a fault rupture through the earth to building response, and the database of near-fault records represents an inhomogeneous mixture of events and site conditions, the overall agreement is encouraging.

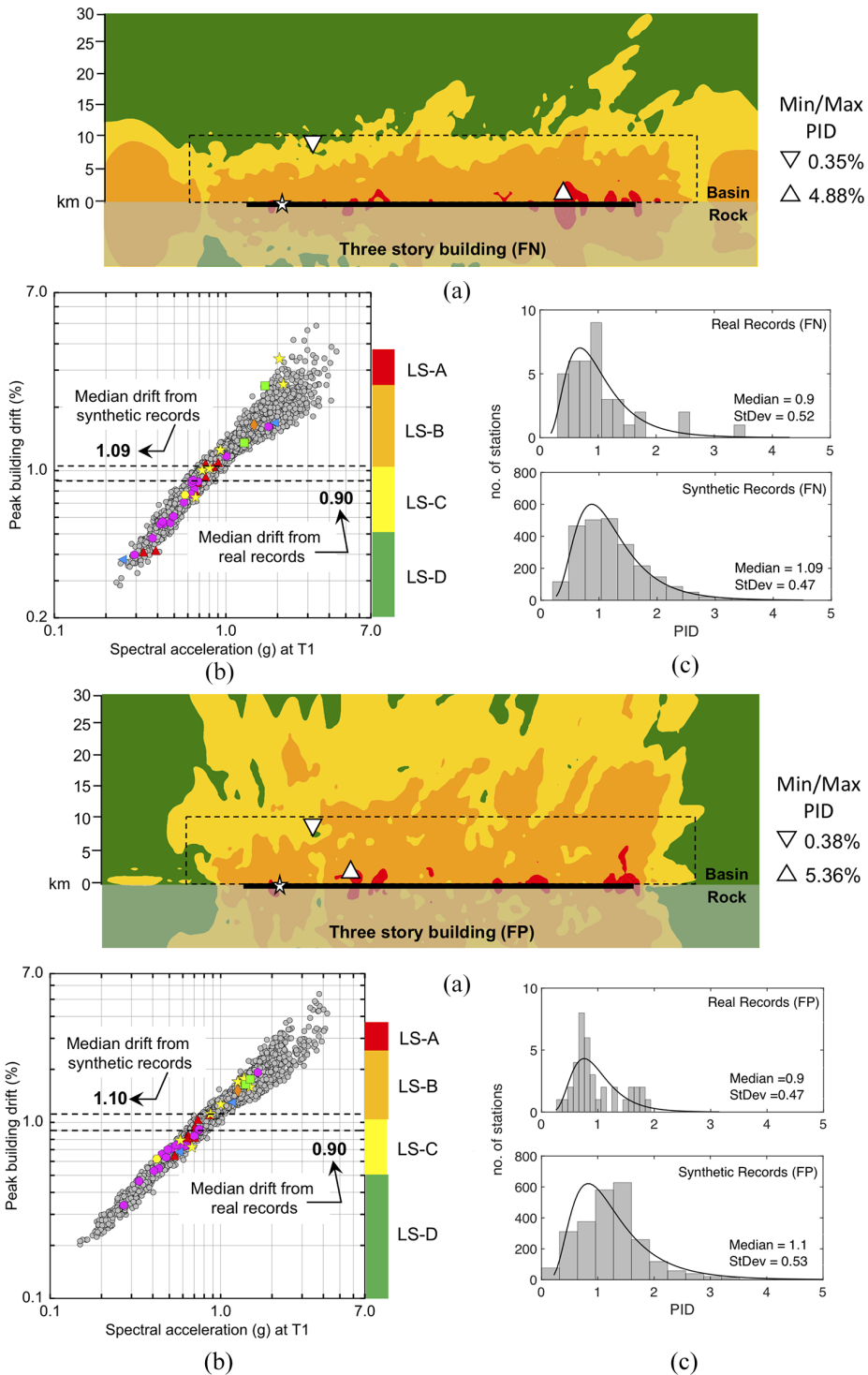


**Figure 8.** Three-story building response for fault-normal and fault-parallel motions: (a) Limit state contours of PID; (b) scatter plot of PID for sites within 10 km of the fault for synthetic (gray circles) and real earthquake (color symbols) records; (c) log-normal PID distributions for real and synthetic ground motions.

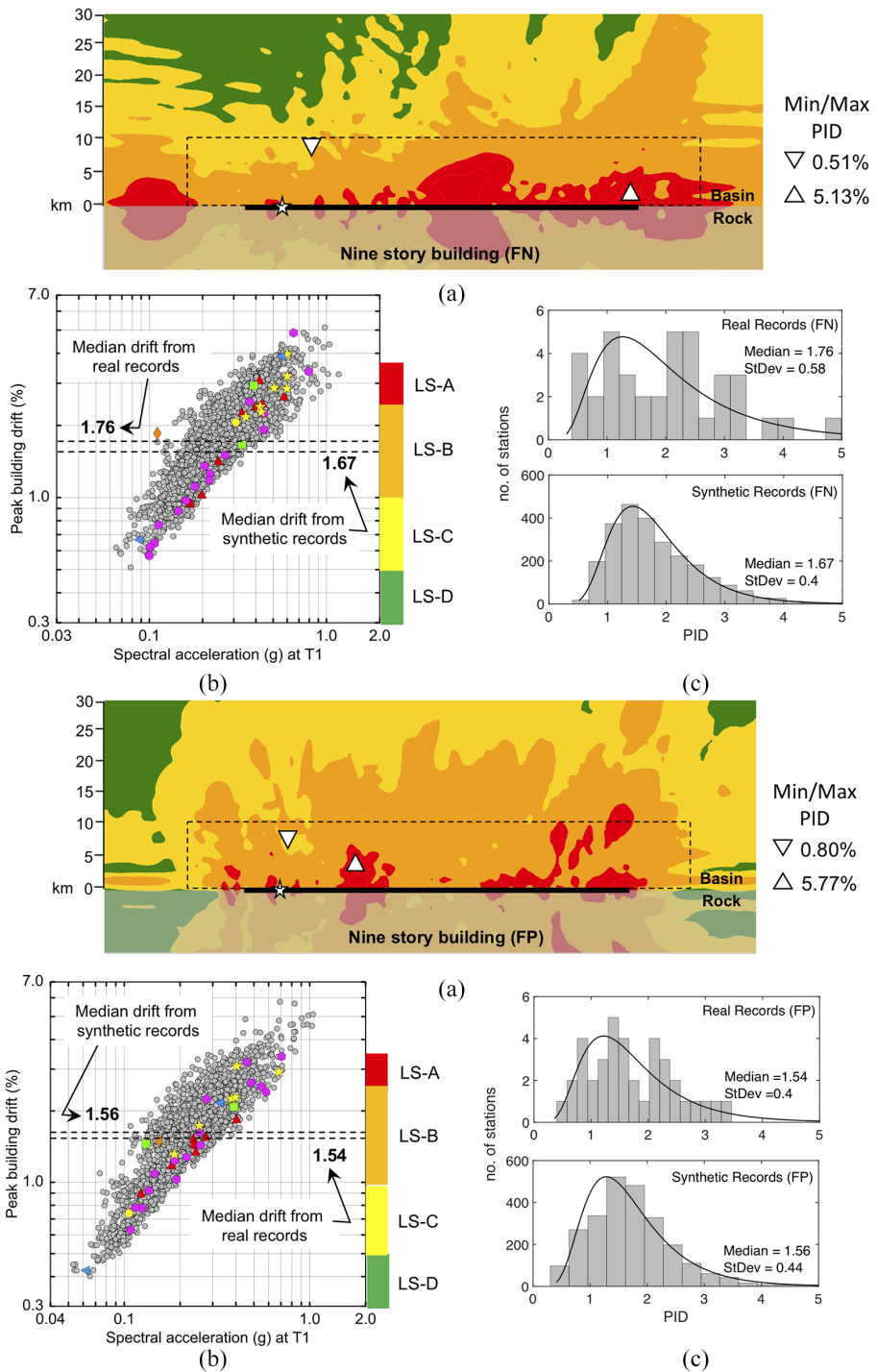


**Figure 9.** Nine-story building response for fault-normal and fault-parallel motions: (a) Limit state contours of PID; (b) scatter plot of PID for sites within 10 km of the fault for synthetic (gray circles) and real earthquake (color symbols) records; (c) log-normal PID distributions for real and synthetic ground motions.



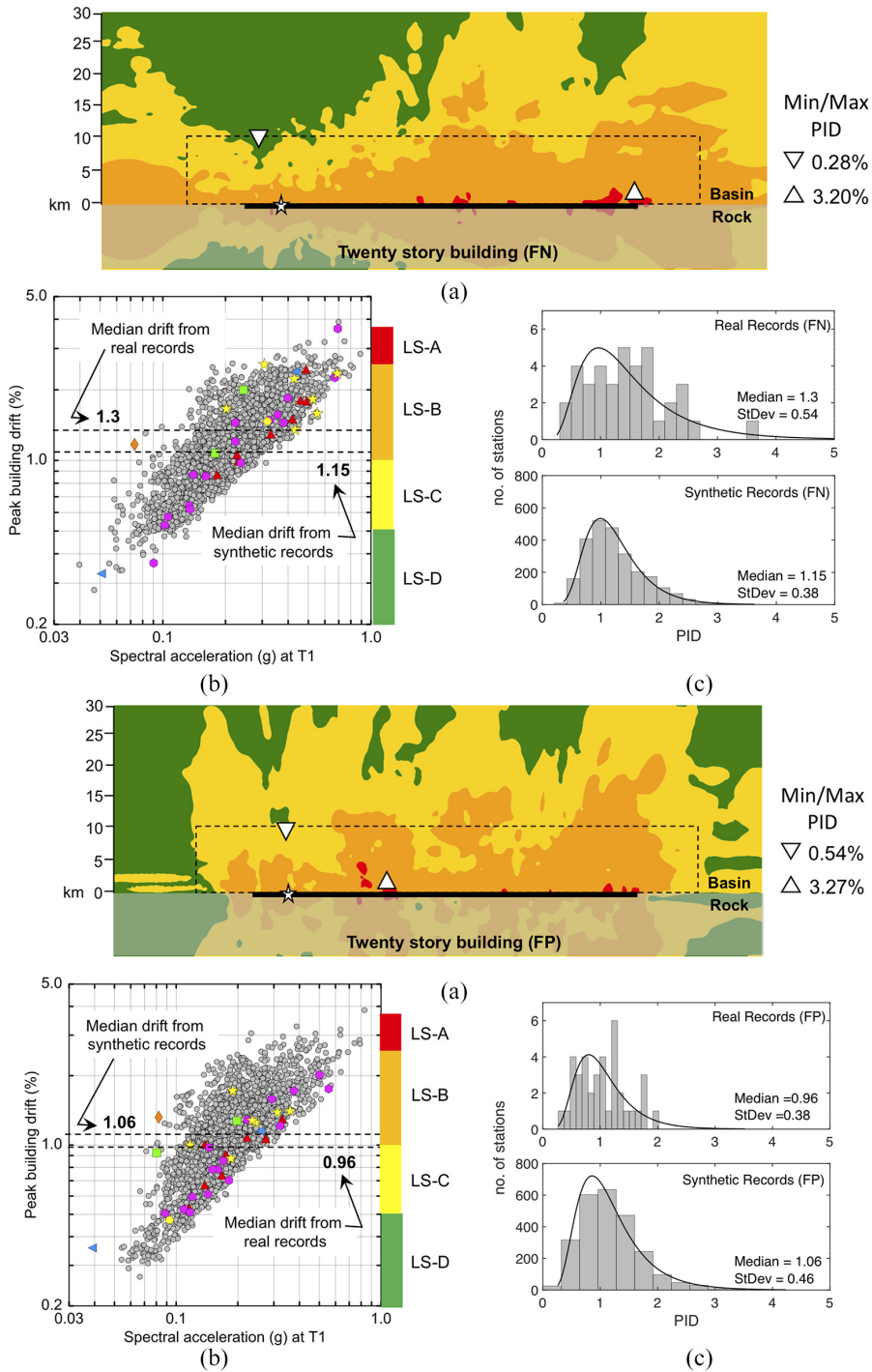


**Figure 10.** Twenty-story building response for fault-normal and fault-parallel motions: (a) Limit state contours of PID; (b) scatter plot of PID for sites within 10 km of the fault for synthetic (gray circles) and real earthquake (color symbols) records; (c) log-normal PID distributions for real and synthetic ground motions.

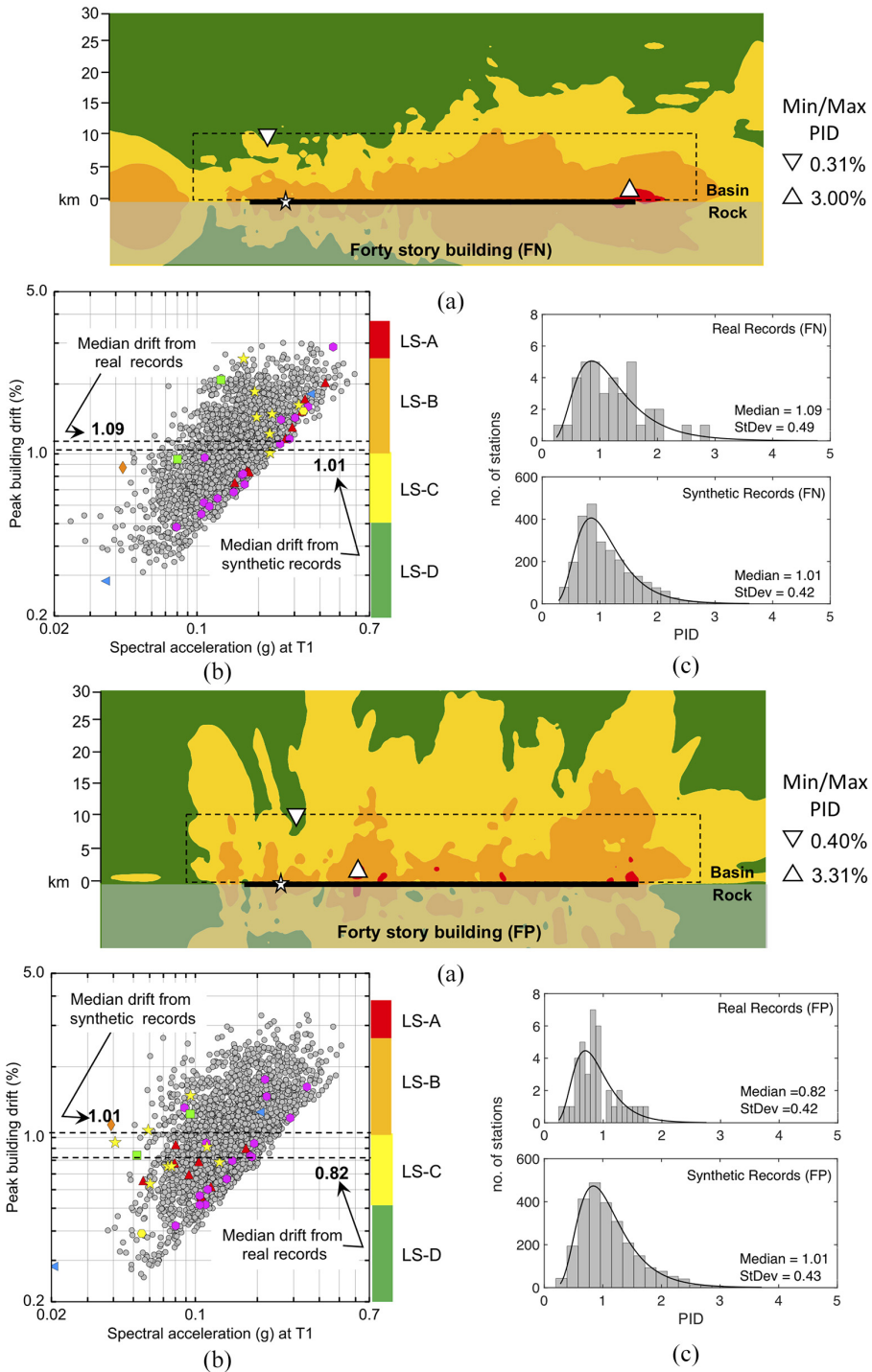


**Figure 11.** Forty-story building response for fault-normal and fault-parallel motions: (a) Limit state contours of PID; (b) scatter plot of PID for sites within 10 km of the fault for synthetic (gray circles) and real earthquake (color symbols) records; (c) log-normal PID distributions for real and synthetic ground motions.

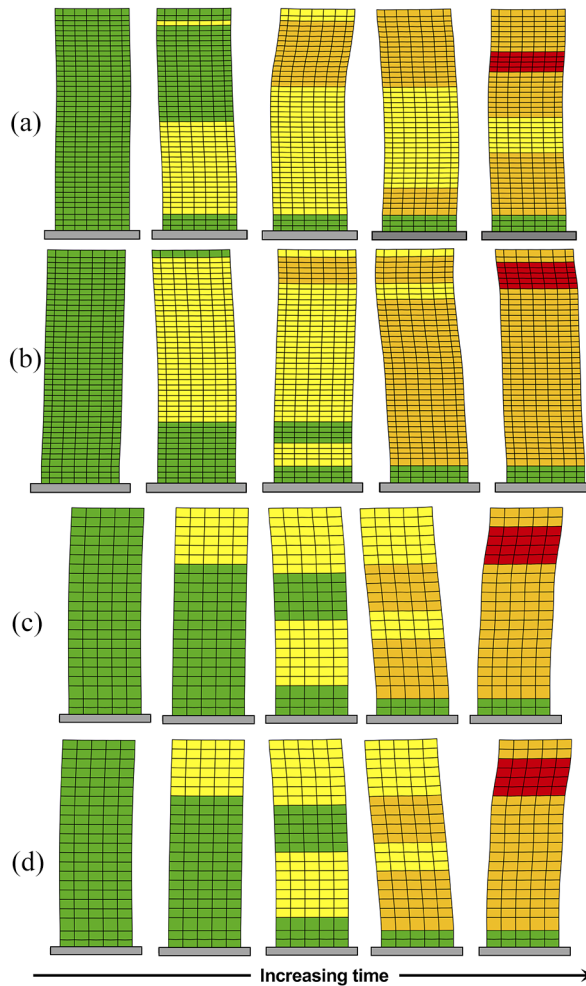


**Figure 12.** Building ASCE 43-05 drift limit state evolution at the location of maximum PID for all sites within 10 km of the fault: (a) Forty-story fault-normal motions; (b) forty-story fault-parallel motions; (c) twenty-story fault-normal motions; (d) twenty-story fault-parallel motions.

The range in simulation-based values of PID for all sites within the 10 km subdomain adjacent to the fault and along the lines parallel to and equidistant from the fault are summarized in Table 7. These results indicate that the seismic demand on a specific building that is located anywhere within 10 km of the fault can vary by as much as a factor of 14, and for a building located at sites equidistant from the fault, the building risk can vary by as much as a factor of 6. This points toward major intra-event variability and the potential for significant site-to-site differences in building response and realized damage for identically designed buildings in the near-field of a major fault. This observation has implications related to efforts to reduce the uncertainty in site hazard and building risk assessments. If the intra-event building response in the near-field can vary by over an order of magnitude dependent on the specific characteristics of the fault rupture, it will be essential to characterize and fully account for the variability controlled by the specific fault-rupture scenario in developing appropriate risk-informed design approaches.

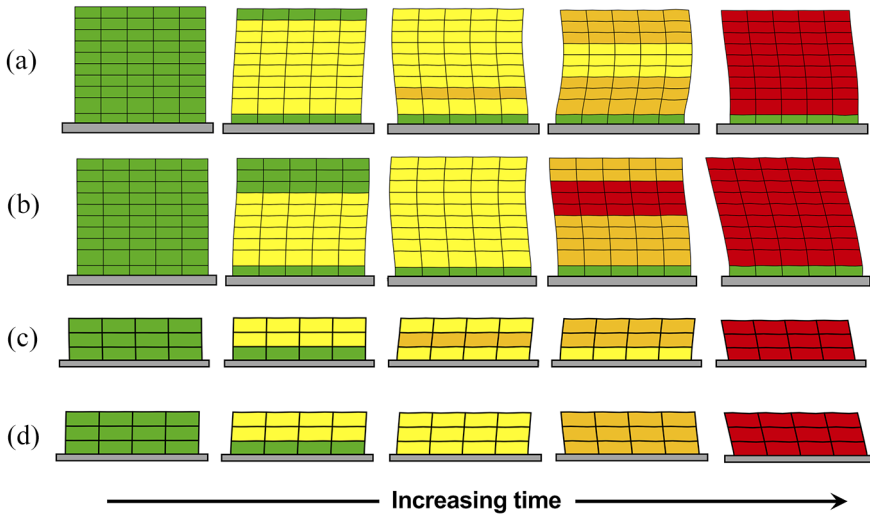


**Figure 13.** Building ASCE 43-05 interstory drift limit state evolution at the site location of maximum PID for all sites within 10 km of the fault: (a) Nine-story fault-normal motions; (b) nine-story fault-parallel motions; (c) three-story fault-normal motions; (d) three-story fault-parallel motions.

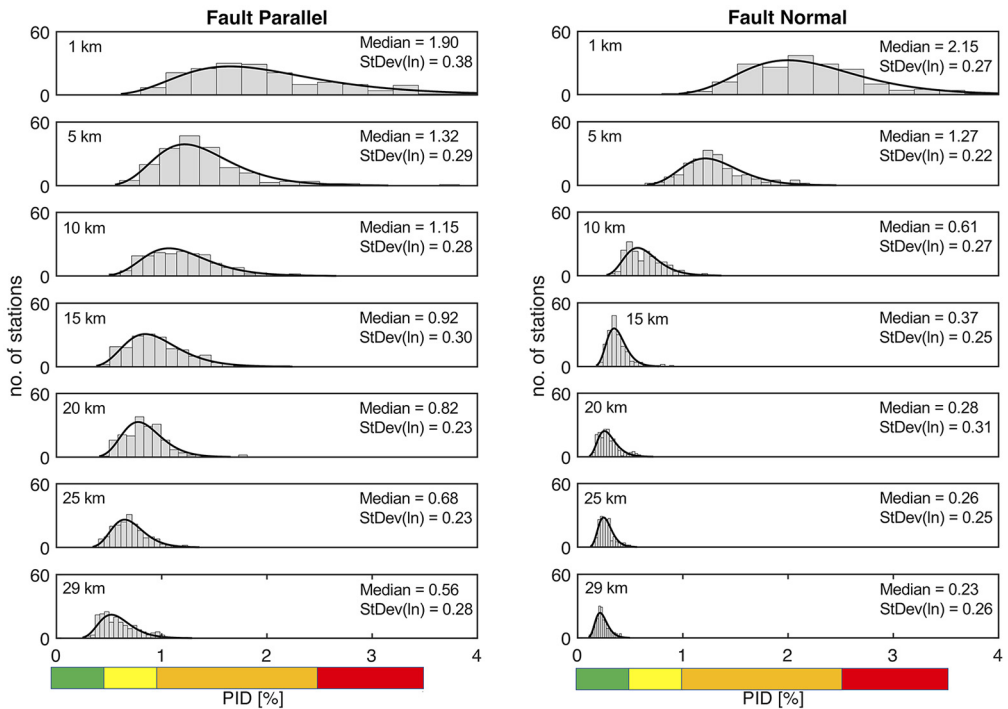


**Figure 14.** Three-story building peak drift variability for sites along lines parallel to, and equidistant, from the fault.

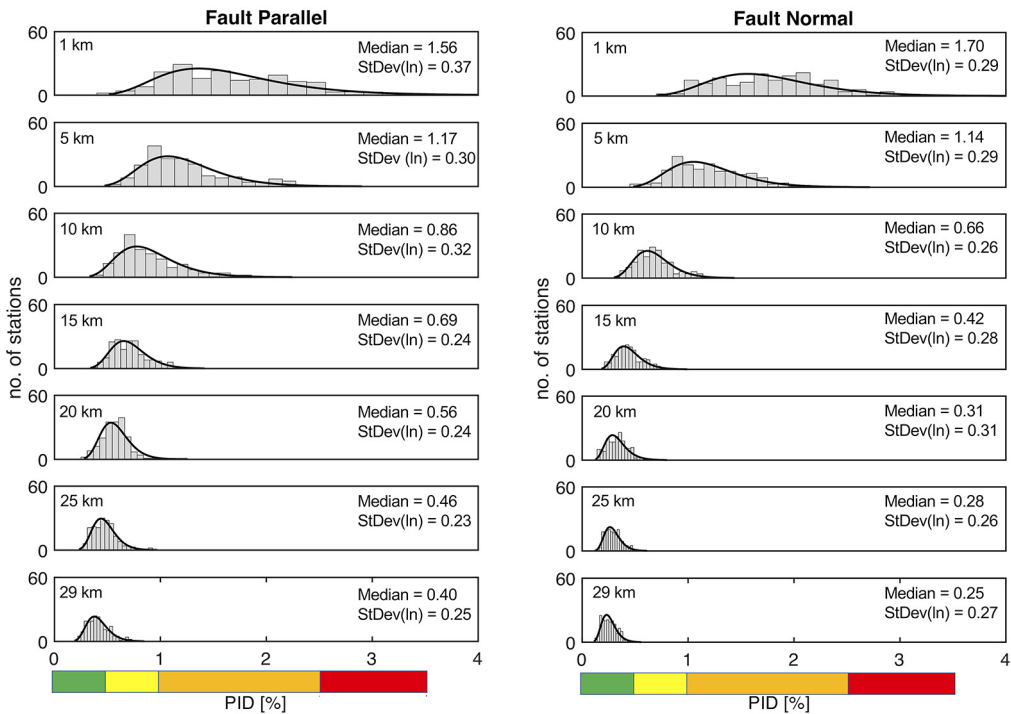


**Figure 15.** Forty-story building peak drift variability for sites along lines parallel to, and equidistant from, the fault.

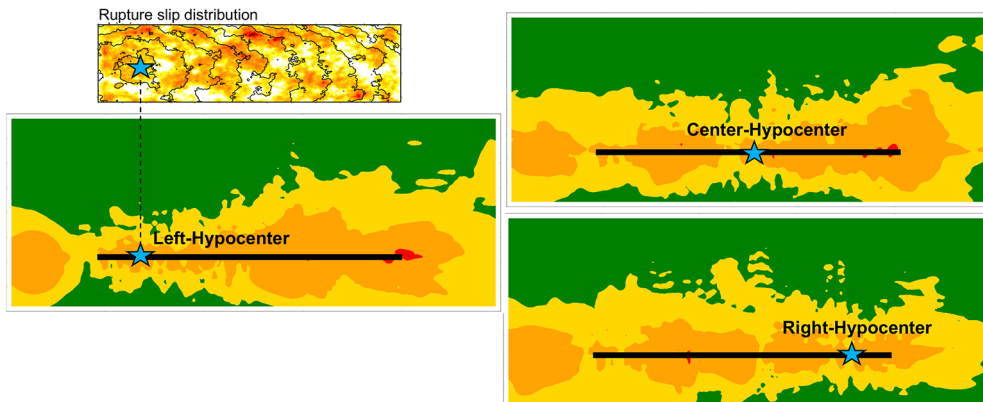


**Figure 16.** Forty-story building limit state contours for fault-normal motions for three different fault-rupture scenarios created by moving the hypocenter location on the rupture plane.

## Inter-event variability of building demand and risk

While the magnitude of a specific future earthquake has some reasonable constraints from geophysical data, very little is known before the earthquake occurs about the precise manner in which a fault will rupture nor the detailed mechanics of the rupture propagation for

**Table 6.** Differences in building median and standard deviation of PID for stations equidistant from the fault located at 1 and 29 km off the fault

Building	Fault-normal component		Fault-parallel component	
	PID <sub>1km</sub> /PID <sub>29km</sub> (on median values)	$\sigma_{1km} - \sigma_{29km}$ (natural log units)	PID <sub>1km</sub> /PID <sub>29km</sub> (on median values)	$\sigma_{1km} - \sigma_{29km}$ (natural log units)
Three story	9.35	0.01	3.39	0.10
Nine story	5.91	-0.01	3.81	0.13
Twenty story	5.59	-0.11	3.73	0.09
Forty story	6.80	0.02	3.90	0.12

**Table 7.** Intra-event ranges of building peak interstory drift (PID) in the near—fault region

Building (component)	10 km	Line	Line	Line	Line	Line	Line	Line
	Box adjacent to fault	1 km from fault	5 km from fault	10 km from fault	15 km from fault	20 km from fault	25 km from fault	29 km from fault
	Min PID	Min PID	Min PID	Min PID	Min PID	Min PID	Min PID	Min PID
	Max PID	Max PID	Max PID	Max PID	Max PID	Max PID	Max PID	Max PID
	Ratio	Ratio	Ratio	Ratio	Ratio	Ratio	Ratio	Ratio
3 (FN)	0.35	0.88	0.71	0.35	0.22	0.16	0.14	0.11
	4.88	4.88	2.10	1.22	0.90	0.58	0.49	0.38
	13.9	5.55	2.96	3.49	4.09	3.64	3.50	3.45
3 (FP)	0.38	0.94	0.61	0.54	0.41	0.52	0.45	0.32
	5.36	4.58	2.51	1.97	1.71	1.31	1.00	1.02
	14.1	4.97	4.11	3.65	4.17	2.52	2.22	3.19
9 (FN)	0.51	1.37	0.98	0.51	0.39	0.23	0.26	0.22
	5.13	5.13	3.69	2.12	1.47	1.13	0.90	0.78
	10.1	3.74	3.77	4.16	3.77	4.91	3.46	3.55
9 (FP)	0.80	1.17	0.85	0.90	0.74	0.66	0.56	0.51
	5.77	5.11	3.80	3.41	2.10	1.53	1.16	1.15
	7.2	4.37	4.47	3.79	2.84	2.32	2.07	2.25
20 (FN)	0.28	1.23	0.66	0.28	0.21	0.17	0.16	0.15
	3.20	2.79	2.21	1.46	1.29	1.02	0.95	0.82
	11.4	2.27	3.35	5.21	6.14	6.00	5.94	5.47
20 (FP)	0.54	0.88	0.68	0.55	0.54	0.43	0.34	0.32
	3.27	3.27	2.73	2.04	1.69	1.00	0.91	0.66
	6.1	3.72	4.01	3.71	3.13	2.33	2.68	2.06
40 (FN)	0.31	0.81	0.51	0.31	0.21	0.15	0.13	0.13
	3.00	2.91	1.90	1.24	0.74	0.48	0.48	0.47
	9.7	3.59	3.73	4.00	3.52	3.20	3.69	3.62
40 (FP)	0.40	0.49	0.56	0.40	0.42	0.36	0.30	0.28
	3.31	3.01	2.18	1.78	1.10	0.83	0.69	0.60
	10.7	6.14	3.89	4.45	2.62	2.31	2.30	2.14

PID: peak interstory drift; FN: fault-normal; FP: fault-parallel.

specific earthquake events. To fully characterize the ground motion hazard and risk at a particular site in the near field, understanding of the full range of variability across a suite of possible encompassing rupture scenarios must ultimately be evaluated. As a first simulation-based look into inter-event variability of building demand, building response characteristics were compared across the three rupture scenarios shown in Figure 2. A

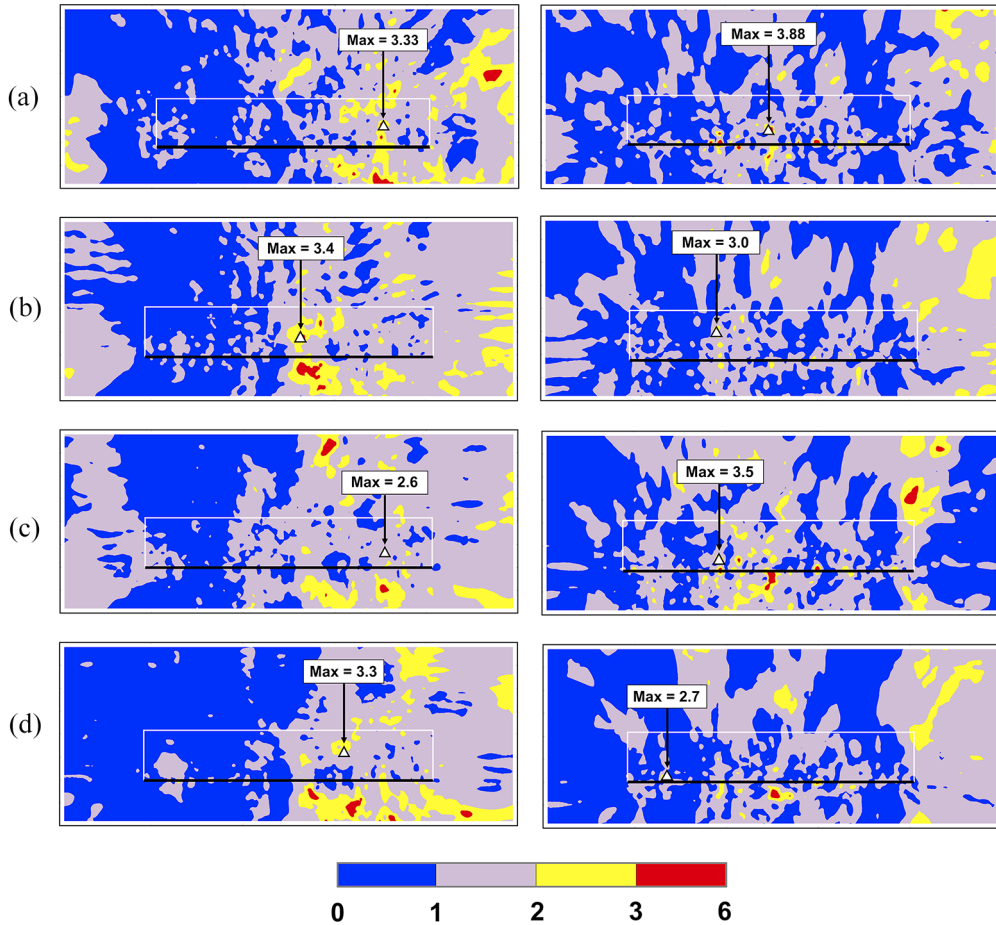


**Figure 17.** Site-by-site ratios of peak interstory drift for left and right rupture scenarios ( $PID_{\text{left hypocenter}}/PID_{\text{right hypocenter}}$ ); (a) Three-story building PID ratios for fault-normal (left) and fault-parallel (right) ground motion components; (b) nine-story building PID ratios; (c) twenty-story building PID ratios; (d) forty-story building PID ratios.

comparison of building limit state contours for a forty-story building for the three different rupture scenarios are shown in Figure 16 to illustrate the change in risk distribution as a function of hypocenter location. Despite the fact that the distribution of fault slip is identical across these rupture scenarios, the change of hypocenter location, and consequently modifications to the local rupture directivity effects, can result in significant changes in the distribution of building response. Comparing the left and right hypocenter simulations, the effect of rupture directivity in the direction of rupture propagation is evident.

To help quantify inter-event building response variability, site-by-site PID ratios were calculated between the left and right hypocenter and left and center hypocenter simulations, respectively. For each site in the regional domain, the ratio— $Ratio = PID_{\text{left hypocenter}}/PID_{\text{second hypocenter}}$ —was computed for all sites in the domain. Contour plots of this ratio are shown in Figures 17 and 18, and the maximum ratio for each building within the

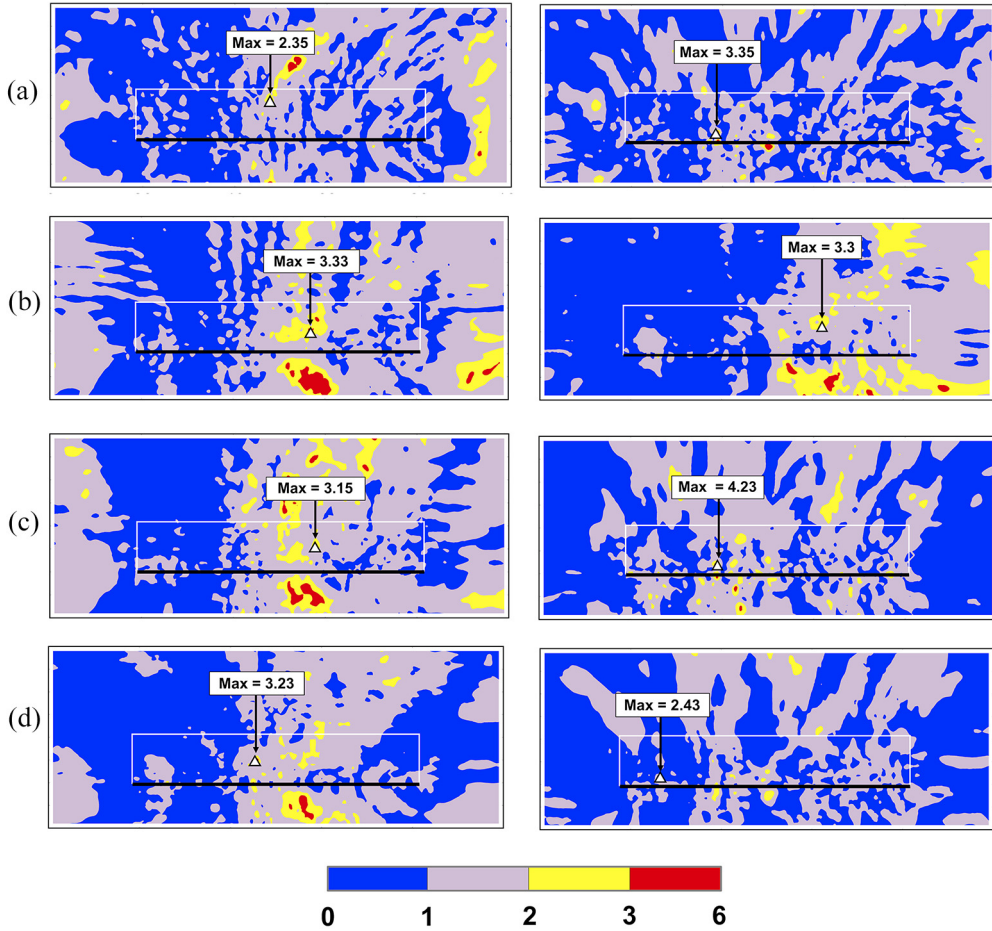


**Figure 18.** Site-by-site ratios of peak interstory drift for left and right rupture scenarios ( $PID_{left\ hypocenter}/PID_{center\ hypocenter}$ ): (a) Three-story building PID ratios for fault-normal (left) and fault-parallel (right) ground motion components; (b) nine-story building PID ratios; (c) twenty-story building PID ratios; (d) forty-story building PID ratios.

near-fault 10 km box in the sedimentary basin is indicated. For all four buildings, there is significant variability in the site rupture scenario ratio with maximum PID ratio ranges between approximately 2.4 and 4.2. In the PID drift ratio plots of Figure 17, the effect of fault directivity is evident as the ratio to the right-hand side of the domain (the location of directivity for the left hypocenter rupture) is consistently larger than one. It is also noted that on the hard rock side of the fault (non-basin), the PID ratios illustrate even large values between 3 and 6.

With the computational speeds that have been achieved with the EQSIM framework (Table 1), comprehensive exploration of the sensitivity of risk distribution to a large number of fault-rupture scenarios and geologic structure realizations for a specific magnitude earthquake is now possible. In the order of 30 such  $M = 7.0$ , 5 Hz resolution, 8.8 billion zone regional-scale rupture scenarios can now be practically computed within two to three



weeks of time on the Cori 30 petaflop platform. The next step in evaluation of EQSIM results is underway with exploration of the inter-event site variability due to a large suite of approximately 30 different fault-rupture characterizations.

## **Discussion and summary**

With the continued rapid advancement in high-performance computer platforms and massively parallel ecosystems, the ability to execute unprecedented simulations of earthquake processes is rapidly advancing. Based on the work described in this article and the companion paper, McCallen et al. (in press), the ability to routinely execute regional-scale simulations for large M7 earthquakes to 5 Hz resolution can readily be performed on today's petaflop systems within entirely manageable compute times that allow exploration of a large number of rupture scenarios and exploration of problem parameter variations. With the pending implementation of the U.S. Department of Energy's exaflop platforms over the next two years, the ability to execute such broadband simulations to 10 Hz, covering a broader spectrum of engineered systems, is within grasp.

The ultimate benefit of realistic fault-to-structure simulations is the potential for reducing uncertainties in regional estimates of the ground motion and infrastructure response through the addition of a large body of synthetic analyses to augment the existing sparse observational database, as well as to allow critical evaluation of traditional assumptions and idealizations. For example, the inherent assumptions of pure vertically propagating shear and compressional waves in traditional fixed-based structural simulations can be evaluated numerically with appropriately coupled regional geophysics and local soil/structure engineering models. Simulations can allow exploration of phenomenon that is either extremely difficult or impossible to fully observed through field instrumentation and thus add new knowledge to our understanding of earthquake hazard and risk. The evaluation of near-fault building response and the large variability of building response for a major earthquake described in this article is one example of the type of information that can be provided from rapidly advancing regional-scale simulation capabilities.

To build the necessary confidence in fault-to-structure simulation results, and to quantify the accuracy of simulation predictions, additional work will be necessary to develop detailed comparisons, including statistical analyses, between simulations and observational data. The first detailed look at fault-to-structure simulations performed here is promising in terms of the ability of large-scale simulations to reflect building response metrics that are in reasonable agreement with building response metrics using existing observational ground motion data. The next phase of work, focusing on a more detailed comparison of simulations and observational data, and the exploration of earthquake rupture inter-event variability through the evaluation of a large suite of rupture scenarios is well underway.

## **Acknowledgments**

The careful review and comments provided by Dr Ricardo Taborda and an anonymous reviewer improved the content of this manuscript and are gratefully acknowledged by the authors.


## **Declaration of conflicting interests**

The author(s) declared no potential conflicts of interest with respect to the research, authorship, and/or publication of this article.

## Funding

The author(s) disclosed receipt of the following financial support for the research, authorship, and/or publication of this article: This research was supported by the Exascale Computing Project (ECP), Project Number: 17-SC-20-SC, a collaborative effort of two U.S. Department of Energy (DOE) organizations—the Office of Science and the National Nuclear Security Administration. This work was performed at the Lawrence Berkeley National Laboratory and the Lawrence Livermore National Laboratory under Contract DE-AC52-07NA27344. Computer access and exceptional support from the National Energy Research Scientific Computing Center (NERSC) at Lawrence Berkeley National Lab is gratefully acknowledged.

## ORCID iD

Arben Pitarka  <https://orcid.org/0000-0001-6026-8859>

## References

- Alavi B and Krawinkler H (2004) Behavior of moment-resisting frame structures subjected to near-fault ground motions. *Earthquake Engineering & Structural Dynamics* 33: 687–706.
- Alexander F, Bell J, Bhattacharjee A, Chen J, Colella P, Daniel D, DeSlippe J, Diachin L, Draeger E, Dubey A, Dunning T, Evans T, Foster I, Francois M, Germann T, Gordon M, Habib S, Halappanavar M, Hamilton S, Hart W, Huang Z, Hungerford A, Kasen D, Kent PRC, Kolev T, Kothe DB, Kronfeld A, Luo Y, Mackenzie P, McCallen D, Messer B, Mniszewski S, Oehmen C, Perazzo A, Perez D, Richards D, Rider WJ, Rieben R, Roche K, Siegel A, Sprague M, Steefel C, Stevens R, Syamlal M, Taylor M, Turner J, Vay J-L, Voter AF, Windus TL and Yelick K (2020) Exascale applications: Skin in the game. *Philosophical Transactions of the Royal Society A* 378: 20190056.
- American Society of Civil Engineers (ASCE) (2005) *Seismic Design Criteria for Structures, Systems and Components in Nuclear Facilities* (ASCE/SEI 43-05). Reston, VA: ASCE.
- Astaneh-Asl A (2018) Designs of 3-, 9-, 20- and 40-story frames. Technical report, Lawrence Berkeley National Laboratory, Berkeley, CA, 25 January.
- Baker J, Lin T, Shahi S and Jayaram N (2011) *New ground motion selection procedures and selected motions for the PEER transportation research program*. Report, PEER 2011/03, March. Berkeley, CA: Pacific Earthquake Engineering Research Center.
- Bijelic N, Lin T and Deierlein G (2019) Evaluation of building collapse risk and drift demands by nonlinear structural analyses using conventional hazard analysis versus direct simulation with CyberShake seismograms. *Bulletin of the Seismological Society of America* 109: 1812–1828.
- Dreger D, Beroze G, Day S, Goulet C, Jordan T, Spudich P and Stewart J (2015) Validation of the SCEC Broadband Platform V14.3 simulation methods using pseudospectral acceleration data. *Seismological Research Letters* 86: 39–47.
- Gazetas G, Garini E, Anastasopoulos I and Georgarakos T (2009) Effects of near-fault ground shaking on sliding systems. *Journal of Geotechnical & Geoenvironmental Engineering* 135: 1906–1921.
- Graves R and Pitarka A (2016) Kinematic ground motion simulations on rough faults including effects of 3D stochastic velocity perturbations. *Bulletin of the Seismological Society of America* 106: 2136–2153.
- Isbilloglu Y, Taborda R and Bielak J (2015) Coupled soil-structure interaction effects of building clusters during earthquakes. *Earthquake Spectra* 31: 463–500.
- Leonard M (2010) Earthquake fault scaling: Self-consistent relating of rupture length, width, average displacement, and moment release. *Bulletin of the Seismological Society of America* 200: 1971–1988.
- McCallen D and Larsen S (2003) *NEVADA—A Simulation Environment for Regional Estimation of Ground Motion and Structural Response*. Directed Research and Development Report UCRL-ID-152115, 3 July. Livermore, CA: Lawrence Livermore National Laboratory.

- McCallen D, Petersson NA, Rodgers A, Pitarka A, Miah M, Petrone F, Sjogreen B, Abrahamson N and Tang H (in press) EQSIM—A multidisciplinary framework for fault-to-structure earthquake simulations on exascale computers Part I: Computational models and workflow. *Earthquake Spectra*.
- Nilsson S, Petersson NA, Sjogreen B and Kreiss HO (2007) Stable difference approximations for the elastic wave equation in second order formulation. *SIAM Journal on Numerical Analysis* 45: 1902–1936.
- Petersson NA and Sjogreen B (2012) Stable and efficient modeling of anelastic attenuation in seismic wave propagation. *Computer Physics Communications* 12: 193–225.
- Petrone F, Wong J, McCallen D and McKenna F (2016) Development of advanced numerical tools for the nonlinear seismic analysis of nuclear systems. *Transactions of the American Nuclear Society* 115: 765–768.
- Petrone, F, Abrahamson, N, McCallen, D, Miah, M (2020) Validation of (not-historical) large-event near-fault ground-motion simulations for use in civil engineering applications. *Earthquake Engineering Structural Dynamics*. Epub ahead of print 30 October 2020. DOI: 10.1002/eqe.3366.
- Pitarka A, Graves R, Irikura K, Miyakoshi K and Rodgers A (2020a) Kinematic rupture modeling of ground motion from the M7 Kumamoto, Japan earthquake. *Pure and Applied Geophysics* 177: 2199–2221.
- Pitarka A, Kawase H, Graves R, Miyakoshi K, Dalguer L, Irikura K, Rodgers A, McCallen D and Wu C (2020b) Rupture modeling for the 2016 Kumamoto, Japan and 2019 Ridgecrest California earthquakes. *Proceedings of the 17th world conference on earthquake engineering*, Sendai, Japan, September 2021, Paper No. C001999.
- Sahin A, Sisman R, Askan A and Hori M (2016) Development of integrated earthquake simulation system for Istanbul. *Earth, Planets and Space* 68: 115.
- Sjogreen B and Petersson NA (2012) A forth order accurate finite-difference scheme for the elastic wave equation. *Journal of Scientific Computing* 52: 17–48.
- Sommerville P (2003) Magnitude scaling of the near-fault directivity pulse. *Physics of the Earth and Planetary Interiors* 137: 201–212.
- Sommerville P and Pitarka A (2006) Differences in earthquake source and ground motion characteristics between surface and buried earthquakes. In: *Proceedings of the eighth national conference on earthquake engineering*, San Francisco, CA, 18–22 April.
- Taborda R and Bielak J (2011) Large-scale earthquake simulation: Computational seismology and complex engineering systems. *Computing in Science and Engineering* 13: 14–26.
- Wu S, Miah M and McCallen D (2019) *Four canonical steel moment frame buildings and inter-code comparisons of nonlinear building response*. Report CCEER 19-05, 9 January. Reno, NV: University of Nevada, Reno Center for Civil Engineering Earthquake Research.
- Zhang W, Esmaeilzadeh Seylabi E and Taciroglu E (2019) An ABAQUS toolbox for soil-structure interaction analysis. *Computers and Geotechnics* 114: 103143.